Physics in Medicine & Biology

IPEM Institute of Physics and Engineering in Medicine

PAPER

On light sharing TOF-PET modules with depth of interaction and 157 ps FWHM coincidence time resolution

M Pizzichemi[1,5], A Polesel[1,2], G Stringhini[1,2], S Gundacker[1,2], P Lecoq[1], S Tavernier[3,4], M Paganoni[2] and E Auffray[1]

[1] CERN, Geneve, Switzerland
[2] University of Milano-Bicocca, Milano, Italy
[3] Laboratorio de Instrumentacao e Fisica Experimental de Particulas, Lisbon, Portugal
[4] Vrije Universiteit Brussel, Brussel, Belgium
[5] Author to whom correspondence should be addressed.

E-mail: marco.pizzichemi@cern.ch

Abstract

The performance of a light sharing and recirculation mechanism that allows the extraction of depth of interaction (DOI) are investigated in this paper, with a particular focus on timing. In parallel, a method to optimize the coincidence time resolution (CTR) of PET detectors by use of the DOI information is proposed and tested. For these purposes, a dedicated 64-channels readout setup has been developed with intrinsic timing resolution of 16 ps FWHM. Several PET modules have been produced, based on LYSO:Ce scintillators and commercial silicon photomultiplier (SiPM) arrays, with 3×3 mm^2 individual SiPM size. The results show the possibility to achieve a timing resolution of 157 ps FWHM, combined with the already demonstrated spatial resolution of 1.5 mm FWHM, DOI resolution of 3 mm FWHM, and energy resolution of 9% FWHM at 511 keV, with 15 mm long crystals of section 1.53×1.53 mm^2 and 3.1×3.1 mm^2. At the same time, the extraction of the DOI coordinate has been demonstrated not to deteriorate the timing performance of the PET module.

1. Introduction

Positron emission tomography (PET) is a clinical and pre-clinical diagnostic technique based on the simultaneous detection of pairs of 511 keV gamma rays emitted from the annihilation of a positron with an electron (Del Guerra *et al* 2016). This measurement is usually performed by several rings of crystal scintillators, such as L(Y)SO:Ce or BGO, coupled with photo-detectors, like photomultiplier tubes (PMTs) or silicon photomultipliers (SiPMs). Pre-clinical and organ-dedicated human PET scanners require very high levels of spatial resolutions, typically in the order of 1–2 mm. This is usually achieved by developing detectors based on scintillators with small cross-section, to improve the localization of the gamma interaction point in the radial coordinate. At the same time, the scanners are designed to be close to the region of interest, to minimize the impact of the acollinearity effect.

The need for high sensitivity imposes the use of long scintillators, potentially giving rise to distortions in the reconstructed images due to parallax effects. Various methods to measure the depth of interaction (DOI) of the gamma rays along the main axis of the scintillators have been developed in order to overcome this limitation. Some examples include, among others, phoswich with pulse-shape discrimination schemes (Karp and Daube-Witherspoon 1987, Ziemons *et al* 2005, Wiener *et al* 2013), independent readout of multiple layers of crystals (Levin 2002), double side readout methods (Bugalho *et al* 2009, Seifert and Schaart 2015), detectors with light sharing DOI encoding (Miyaoka *et al* 1998, Liu *et al* 2001, Yang *et al* 2009, Ito *et al* 2010, 2013), monolitic scintillators (Borghi *et al* 2016, Marcinkowski *et al* 2016), phosphor coated scintillators (Berg *et al* 2016, Kwon *et al* 2016), sub-surface laser engraving (Uchida *et al* 2016, Bläckberg *et al* 2018), double side G-APD cross-strip readout (Kolb *et al* 2014), and wavelength discrimination (Shimazoe *et al* 2016). We recently proposed a method to obtain DOI information with high resolution, in the order of 3 mm FWHM, based on a simple light sharing and re-circulation scheme in single side readout and without the need for one-to-one coupling between crystals and

detectors (Pizzichemi *et al* 2016, Stringhini *et al* 2016). Due to the limitations of the acquisition setup, at that time we were not able to investigate fully the timing capabilities of this method, and especially the influence of DOI on coincidence time resolution (CTR).

Measuring the time of flight (TOF) of gamma rays allows to restrict the point of annihilation of the positrons to a smaller segment along the lines of response (LORs), which has been demonstrated to sharply increase in the signal to noise ratio (SNR) of reconstructed images (Conti 2011). The gain in SNR of a TOF PET system, compared to a non-TOF PET one, is directly proportional to the physical dimension of the region of interest under study and proportional to the CTR. Typical timing resolutions of currently available whole-body PET scanners are in the order of 215–315 ps FWHM (Miller *et al* 2015, van Sluis *et al* 2019). It is clear that smaller objects, like the ones investigated in pre-clinical imaging or in organ-dedicated PET systems, require even better TOF resolutions to reach the same levels of SNR gain. The first goal of this work is therefore to assess the timing resolution that can be achieved with the proposed DOI method, in order to determine if it can be successfully adopted for the development of a new generation of high resolution PET scanners.

Furthermore, nowadays the direction of research in PET is more and more pointing towards a new frontier in terms of timing resolution, with the ultimate goal set to 10 ps FWHM CTR (Lecoq 2017). The reason for this can be found in the possibility to access directly the information on the 3D position of the positron annihilation point, offering novel strategies in the reconstruction or correction algorithms (Defrise *et al* 2012). Reaching such a high level of CTR will require a great improvement in the performance of every element of the PET acquisition chain. At the same time, it is well known that the uncertainty on DOI introduces a bias on timing measurement, because of the mismatch in the speed of propagation in dense scintillators between gamma rays and optical photons. The magnitude of this bias has been evaluated in the order of 150–200 ps (Moses and Derenzo 1999, Shibuya *et al* 2008) for long (15–20 mm) LYSO:Ce scintillators. There have been several attempts to integrate the DOI smearing effect on timing into the analytical modeling of CTR in PET detectors (Gundacker *et al* 2014, Vinke *et al* 2014). In particular, it has been demonstrated that while in current LYSO/SiPM detectors the DOI blur on timing measurements does not significantly affect CTR, its impact would be significant for long, near-ideal scintillator detectors, preventing the achievement of CTR values below 50 ps FWHM (Toussaint *et al* 2019). As a consequence, the goal of 10 ps FWHM timing resolution cannot be reached in PET systems based on long scintillators without some knowledge on the DOI position of the incoming gamma rays. The computation of DOI is therefore expected to become mandatory also for whole-body PET scanners. Obviously, this DOI information will have to be extracted without affecting the intrinsic CTR of the system. Therefore the second aim of this work is to demonstrate that the light sharing and re-circulation scheme that we proposed does not degrade the timing information.

2. Materials and methods

Throughout this paper, we refer in general to a *module* as a combination of scintillators and photo-detectors. In section 2.1, a configuration to produce a PET module with DOI capabilities is described, based on depolished crystals and a light sharing scheme. Subsequently, a procedure to optimize the extraction of timing information and improve CTR with DOI is proposed in section 2.2. To evaluate the impact on timing resolution of the DOI extraction method, another module configuration will be presented in section 2.3, similar to the one illustrated in section 2.1, but based on polished scintillators and without light sharing. This configuration does not allow for the computation of DOI, but it is known to yield optimal energy and timing resolutions, and will therefore be used as a reference. Finally, the experimental setup and the procedure followed to evaluate the performance of the modules under study are presented in sections 2.4 and 2.5.

2.1. DOI modules

DOI information can be extracted in a PET module by coupling an array of $M \times M$ photo-detectors on one side of a matrix of $N \times N$ scintillators, as shown in figure 1. In general, $N \geqslant M$, i.e. one or more crystals can be coupled to the same photo-detector, without affecting the validity of the method. The four lateral surfaces of each scintillator are depolished, while the two remaining sides are polished. The scintillators are separated from each other by foils of reflective material. The side of the scintillator array opposite to the photo-detectors is coupled to a light guide made of glass. For both the scintillators-photodetectors and scintillators-glass interfaces, the optical coupling is obtained by means of optical grease or transparent adhesive, to maximize optical transmission. Finally, a foil of reflective material is placed in dry contact on the back of the light guide. When a gamma ray interacts at a given DOI of a pixel in the scintillator array, the light produced propagates in the crystal and is eventually emitted both from the scintillator side coupled to the photo-detector and from the opposite one (red and blue arrows, respectively, in figure 1). Because of the optical depolishing of the lateral surfaces of the crystal, the ratio of the amount of light emitted by the two ends of the scintillator depends on the gamma interaction position along the crystal (Vilardi *et al* 2006, Trummer *et al* 2009).
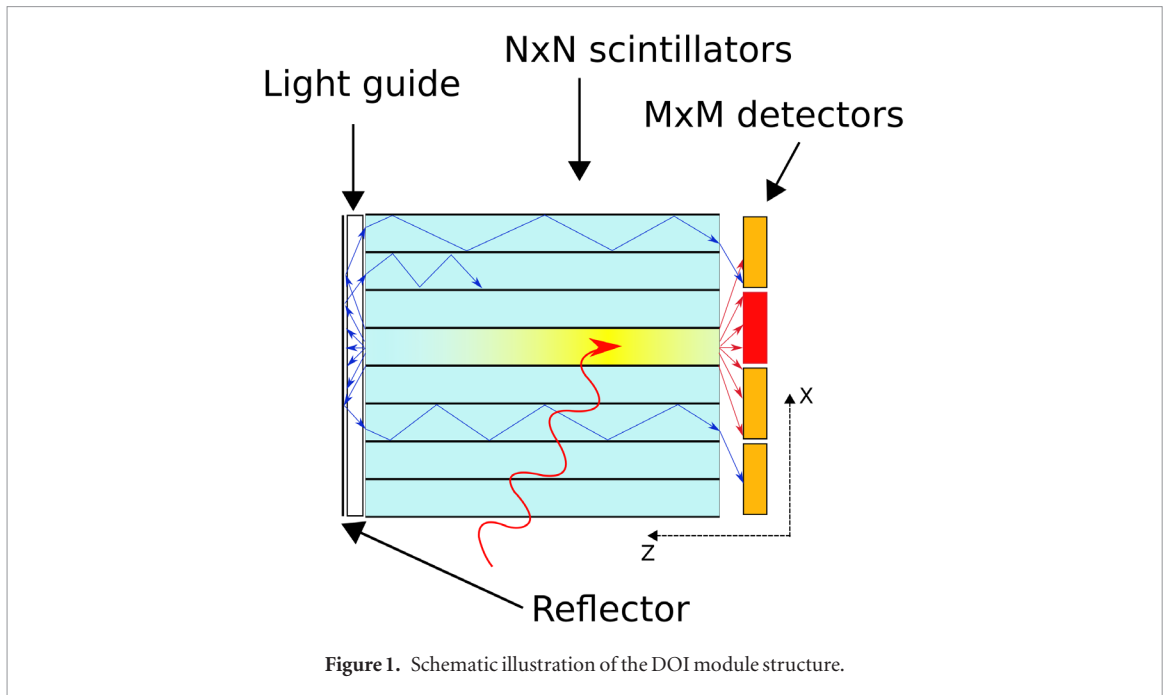
Figure 1. Schematic illustration of the DOI module structure.

Thanks to this light re-circulation scheme, a certain number K of photo-detectors is hit by the photons generated by the scintillation event. We denote these photo-detectors as D_i, with $i = 1, 2, \ldots, K$. Their physical position in a $x - y$ plane parallel to the photo-detector array is expressed in terms of the coordinates x_i and y_i of their centers. For each D_i, the amount of light collected by the photo-detector is denoted as p_i, and the measured time of detection as t_i. In what follows, the index $i = 1$ always refers to the photo-detector directly coupled to the crystal where the interaction occurred. For each scintillation event, this photo-detector D_1 can easily be identified, since it is expected to measure the maximum amount of light $p_1 = p_{max}$. The total amount of light collected by all the K photo-detectors can be calculated simply as

$$P = \sum_{i=1}^{K} p_i. \tag{1}$$

Given these definitions, it has been demonstrated that for each scintillation event, the quantities

$$u = \frac{1}{P} \sum_{i=1}^{K} p_i x_i \quad , \qquad v = \frac{1}{P} \sum_{i=1}^{K} p_i y_i \quad , \qquad w = \frac{p_{max}}{P} \tag{2}$$

allow at the same time for the correct identification of the crystal where the gamma interaction occurred, and for the computation of the DOI coordinate with a resolution that has been estimated in the order of 3 mm FWHM. Furthermore, a fast calibration procedure has been proposed and validated (Stringhini *et al* 2016).

2.2. Method for timing optimization

If we consider the DOI module described in section 2.1, a simple estimation on t_{in}, the time of entrance of the incoming gamma ray in the crystal of interaction, would be provided by t_1, i.e. the time of detection for the photo-detector D_1 coupled to the crystal itself. Anyway, because of the light sharing mechanism, only part of the light produced in the scintillation process reaches the photo-detector D_1. As shown in figure 1, also the photo-detectors adjacent to D_1 are hit by the optical photons, mainly by the light spreading through the back of the module. As a result, in general the timestamps of these photo-detectors will be seen as delayed with respect to t_1. Furthermore, it is reasonable to expect that this delay depends on the DOI position, since it is proportional to the difference between the mean path that the optical photons have to travel to reach the photo-detectors. We can therefore state that a relation

$$g_i(w) = [t_i - t_1](w) \tag{3}$$

between the average delay of the ith photo-detector with respect to D_1 and the DOI coordinate w exists, for each D_i. For symmetry, this is valid also in the limit case of D_1, where of course $g_1(w) \equiv 0$.

The $g_i(w)$ relations can be measured directly with a procedure that will be described in section 2.5, where the delay $(t_i - t_1)$ is plotted, event by event, against w for each $D_{i \neq 1}$, after photopeak selection in a given crystal. This allows to build a series of 2D histograms (see for example the one in figure 2), whose profiles provide an experimental measurement of the relations (3). Once these relations are known, for any event of all subsequent
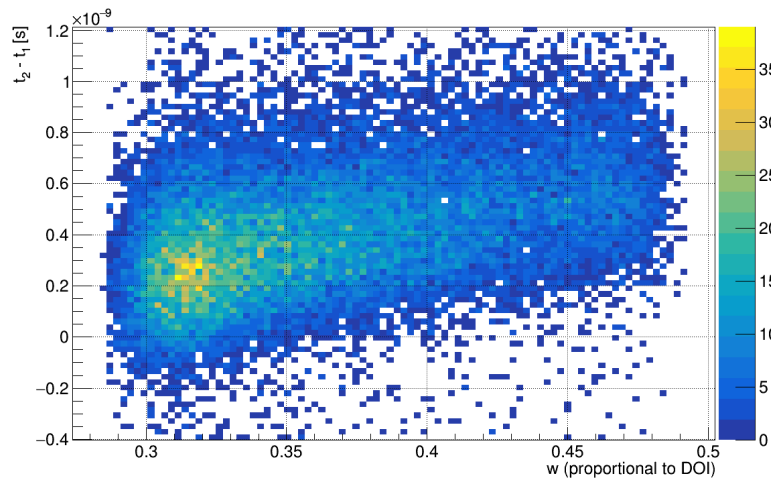
Figure 2. Example of the scatter plot of the delay $(t_2 - t_1)$ versus w, between two photo-detectors D_1 and D_2, measured for events confined in the photopeak of an individual scintillator of one of the modules investigated in this study.

acquisitions it is possible to obtain K independent estimations of t_1, simply subtracting from t_i the expected delay from D_1, calculated at the w of that specific event

$$t_1^{(i)} = t_i - g_i(w). \tag{4}$$

These measurements can be combined to get the best estimator of t_1, as follows

$$\hat{t}_1 = \frac{\sum_{i=1}^{K}(1/\sigma_i^2) \cdot t_1^{(i)}}{\sum_{i=1}^{K}(1/\sigma_i^2)} \tag{5}$$

where the weights σ_i are obtained from the width of the histograms of the $t_1^{(i)}$ measurements, acquired during calibration, evaluated in the w of the event.

In the same calibration run, the difference between t_1 and the timestamps of the photo-detector coupled to an external, fast reference crystal, t_{ref}, is plotted against w, for several events in the photopeak of a given crystal. A clear correlation is observed, as shown in figure 3, reflecting the impact of the DOI coordinate on timing. From the profile of such scatter plot, it is possible to obtain an experimental measurement of $d(w)$, i.e. the average delay expected, as a function of w, between t_1 and a fixed external reference. For each event localized in the same crystal of any subsequent acquisition, the best time estimator of t_{in} can be found as

$$\hat{\theta}_{in} = \hat{t}_1 - [d(w_0) - d(w)] \tag{6}$$

i.e. correcting $\hat{t}_1$ by the difference between the average delay expected at the value of w measured for that event and the average delay that would be measured at a fixed reference DOI position, expressed by w_0. The width of the delay histograms constructed using $\hat{\theta}_{in}$ should therefore represent the best possible CTR achievable by the DOI module under study.

2.3. Reference modules configuration

A PET module configuration without DOI capabilities is also studied in this work. It is based on the typical structure of modules used nowadays in PET scanners, and will be useful for comparison with the DOI module proposed. The structure of a reference module is very similar to the one of a DOI module. The only differences are the use of fully polished scintillators, and the absence of a light guide, as shown in figure 4. As a result, light sharing is extremely reduced and no DOI capabilities are expected. On the other hand, polished scintillators are known to yield the best results in terms of timing and energy resolutions.

2.4. Experimental setup

A total of eight modules have been assembled for testing in this work. As reported in table 1, they are divided in two groups of four DOI modules and four reference modules, assembled following the configurations described in sections 2.1 and 2.3, respectively.

Each module is assigned a unique ID, $X.Y.Z$, where X denotes the module type (D = DOI module, R = reference module), Y the number of scintillators in the LYSO:Ce array, and Z the item number (1 or 2) between identical arrays. All modules are based on LYSO:Ce crystal arrays produced by Crystal Photonics Inc., United States (see figure 5). In particular, the lateral surfaces of each scintillator in the arrays used to assemble DOI modules
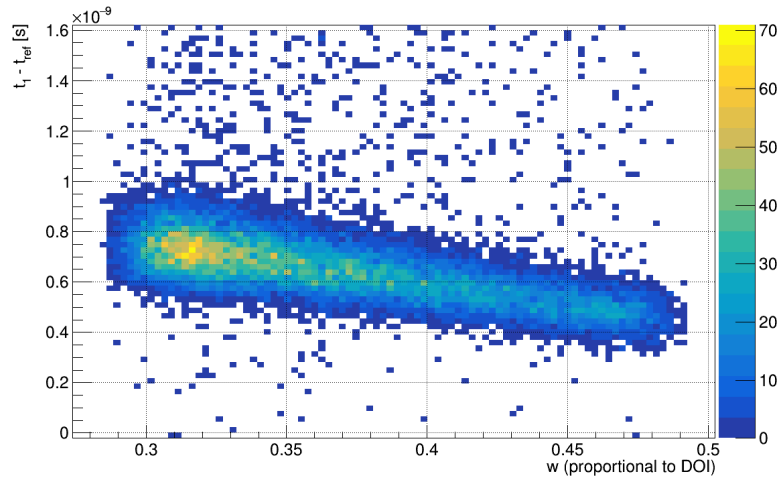
Figure 3. Example of the scatter plot of $t_1 - t_{ref}$ versus w, measured for events confined in the photopeaks of an external reference detector and of an individual scintillator of one of the modules investigated in this study.
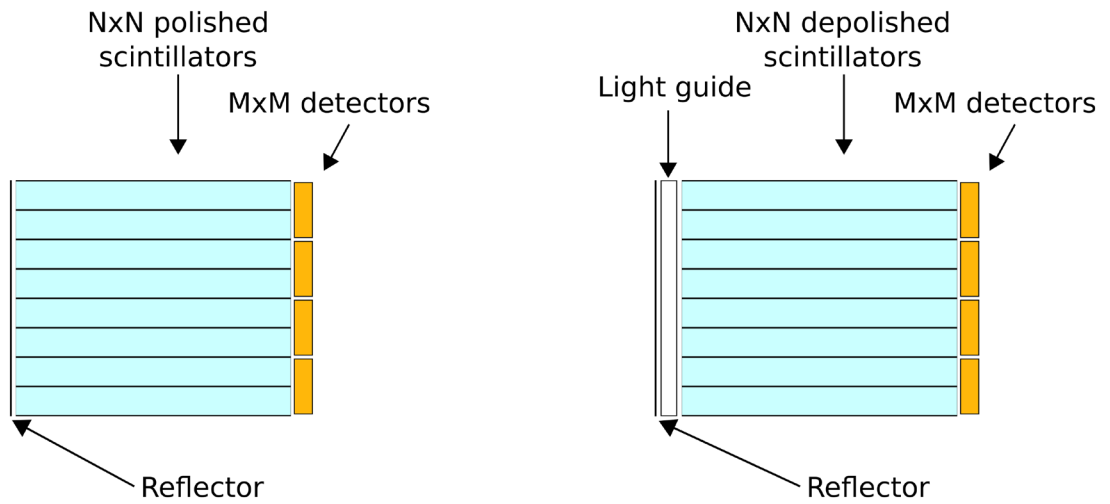

Figure 4. Comparison between the structure of reference modules (left) and DOI modules (right), in this case for 8×8 crystal arrays. The two structures differ only in the presence of a light guide, and the depolished surface finishing in the DOI modules.

Table 1. Type, structure and relevant characteristics of the eight modules investigated in this work.

Type	Sample ID	Crystal size (mm³)	Crystal arrangement	Lateral surfaces finishing	Light guide
DOI	D.64.1	$1.53 \times 1.53 \times 15$	8×8	Depolished	Yes
	D.64.2				
	D.16.1	$3.1 \times 3.1 \times 15$	4×4	Depolished	Yes
	D.16.2				
Reference	R.64.1	$1.53 \times 1.53 \times 15$	8×8	Polished	No
	R.64.2				
	R.16.1	$3.1 \times 3.1 \times 15$	4×4	Polished	No
	R.16.2				

are depolished, while each crystal is fully polished in the case of reference modules. Foils of enhanced specular reflector (ESR, by 3M), 70 μm thickness, are inserted between the crystals and build the matrix structure, acting also as a wrapping material. The reflectors are not bonded to the scintillators, and therefore a thin air gap remains between ESR and crystals. The modules are wrapped with a layer of Teflon, to ensure mechanical stability. The arrays are coupled by means of optically clear adhesive (OCA 8172CL, by 3M), 50 μm thickness, to a TSV photo-detector array produced by Hamamatsu, model S13361-3050-AE-04 (see figure 5), made of 16 multi-pixel photon counters (MPPCs), each with 3×3 mm² active area. In DOI modules, a light guide made of glass,
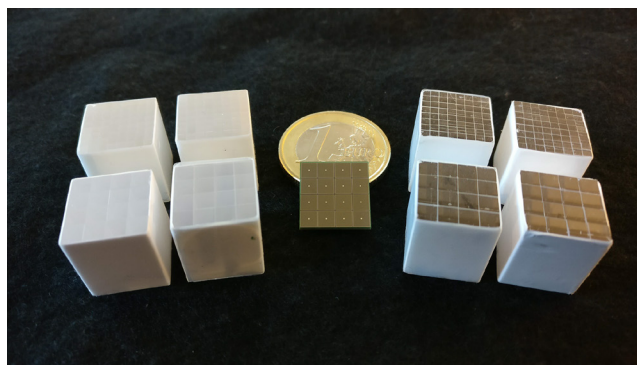
Figure 5. Scintillator and photo-detector arrays used in this study. All scintillator arrays are made of LYSO:Ce, and produced by Crystal Photonics Inc., United States. In the four on the left, the lateral surfaces of each scintillator is depolished. In the others, all crystal surfaces are fully polished. Arrays on the top raw are made of 64 scintillators, while on the bottom by 16. In the center, one Hamamatsu S13361-3050-AE-04 photo-detector array.

$12.8 \times 12.8 \times 1 \, \text{mm}^3$, is coupled by means of optically clear adhesive (OCA 8146-5, by 3M), 125 μm thickness, to the scintillator array, and covered with a foil of ESR in dry contact. In reference modules no light guide is used, and the foil of ESR is placed directly on the scintillator array.

The first two modules in both DOI and reference groups are based on $1.53 \times 1.53 \times 15 \, \text{mm}^3$ scintillators and present a 4-to-1 coupling between crystals and photo-detectors (see figure 6, left). These characteristics make them particularly interesting for the study of the possible development of pre-clinical and organ dedicated PET systems. The remaining modules, instead, are more suited for studying the performance of the DOI timing correction method applied to whole-body PET scanners, especially towards the 10 ps FWHM CTR goal, being made of $3.1 \times 3.1 \times 15 \, \text{mm}^3$ scintillators, and with 1-to-1 coupling (figure 6, right).

In order to extract the DOI coordinate with the method described in section 2.1, an accurate evaluation of the amount of light hitting each photo-detector is required. This can be achieved by integrating the electrical pulses generated by each photo-detector when hit by the scintillation light. At the same time, evaluating timing and performing the correction procedure proposed in section 2.2 requires parallel multichannel readout with fast electronics. A proper acquisition system has been developed accordingly (see figure 7), based on two identical custom developed front end boards (FEBs) and a combination of CAEN VME digitizers. Each FEB (see figure 8) can host up to two Hamamatsu S13361-3050-AE-04 MPPC arrays, for a total of 32 MPPCs, through two Samtech connectors. Event by event, the signal generated by each photo-detector is split in two parts. One is amplified and fed directly to one channel of a 64ch VME V1740D CAEN module, that digitizes and integrates the pulse shape. The other is routed to one input channel of a NINO-32 amplifier-discriminator board (Anghinolfi *et al* 2004), that produces a square wave subsequently digitized by one channel of two fast 32ch VME V1742 CAEN modules (LSB 200 ps). The timestamp of the photo-detector is calculated by the crossing of the rising edge of this square wave with a fixed threshold. Upon every trigger event, therefore, a value of the integrated charge deposited and a timestamp is stored for any photo-detector connected to the FEBs. It has to be noted here that the value of integrated charge obtained from each MPPC is corrected to compensate for the well-known saturation effect of SiPMs due to the finite number of microcells present in the photo-detector, with a standard procedure that involves the use of several gamma sources (Otte *et al* 2005). In particular, each SiPM is coupled to a 4×4 LYSO:Ce array made of polished scintillators, the measured integrated charge is evaluated for the photopeaks corresponding to the gamma emissions of ^{22}Na, ^{137}Cs, ^{57}Co, ^{60}Co and ^{176}Lu sources, and a calibration curve is derived.

In order to evaluate the timing performance of the acquisition system, the signal of a single Hamamatsu S13360-3050-PE photo-detector (active area $3 \times 3 \, \text{mm}^2$), coupled to an individual LYSO:Ce crystal (Crystal Photonics Inc., $1.7 \times 1.7 \times 3.0 \, \text{mm}^3$) has been sent by means of a custom adapter to several pairs of channels belonging to the same FEB. The width of the histogram of the difference between the timestamps recorded by the two channels, upon excitation with an external 511 keV source, provides a measurement of the intrinsic timing resolution of the setup. With this method, the average timing resolution of the acquisition system has been evaluated to be 16 ps FWHM, comparable to measurements obtained with a NINO8 board and a fast oscilloscope (Gundacker *et al* 2016). Since the expected timing performance of the LYSO:Ce modules under test is estimated to be roughly one order of magnitude greater, the contribution to CTR of the acquisition system can be considered negligible and will not be subtracted from the final results.

Although the readout system allows to acquire directly in coincidence two modules, one against the other, in order to properly assess the individual performance of each sample in table 1, and especially to carefully study the validity of the proposed timing correction method, a dedicated experimental setup, based on a single channel external reference detector, common to all modules, has been prepared (see figure 9). One module is connected
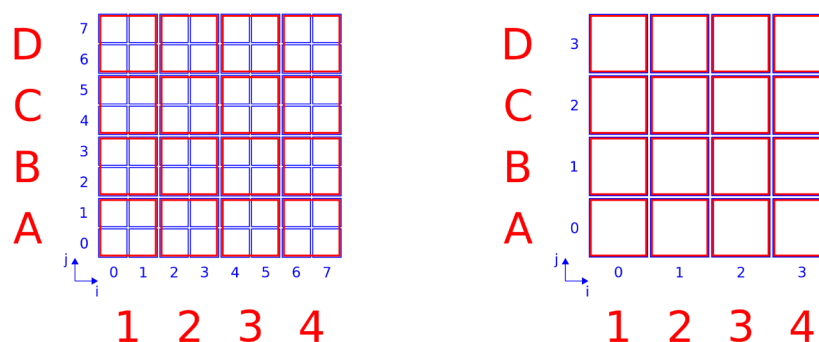
Figure 6. Coupling between crystals (blue) and MPPCs (red), for *X.64.Z* (left), and *X.16.Z* (right) modules. The labeling convention for photo-detectors and crystals is also reported.
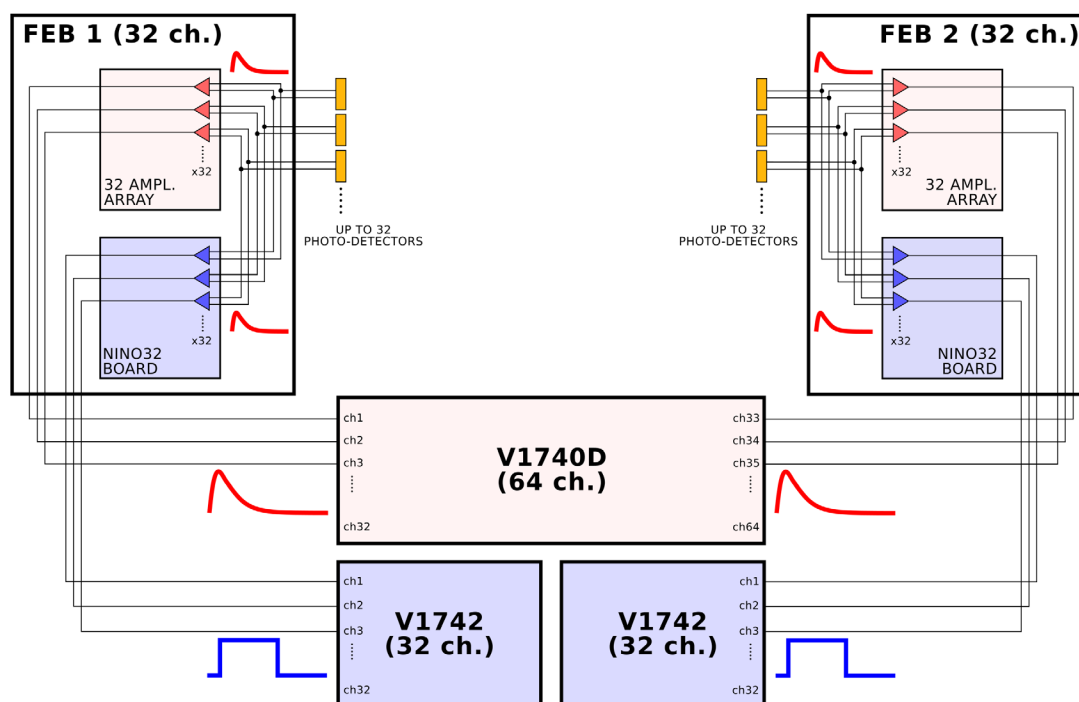

Figure 7. Schematics of the acquisition system developed for this work, based on two custom developed FEBs, one CAEN V1740D and two CAEN V1742 digitizers. Up to 32 photo-detectors can be connected to each FEB. The signal from each photo-detector input is split in two. One side is amplified and fed to the V1740D digitizer, that measures the charge deposited on the photo-detector, by pulse shape integration. The other is routed to the NINO32 chip, producing a square wave that is sent to one of the two V1742 modules for timestamp calculation. For each event, therefore, up to 64 charges and 64 timestamps can be measured in parallel.

to one of the two FEBs. A single Hamamatsu S13360-3050-PE photo-detector (active area 3×3 mm^2) is plugged via a custom adapter into the opposite FEB, and coupled to an individual LYSO:Ce reference crystal, produced by Crystal Photonics Inc., United States, of dimensions $1.7 \times 1.7 \times 3.0$ mm^3. Finally, a ^{22}Na source is placed between the modules and the reference crystal and the acquisition is performed in coincidence.

The characterization of the modules in terms of timing resolution with this setup requires evaluating and subtracting the contribution to CTR due to the reference detector. This has been measured as follows. First, two identical crystals, each $2 \times 2 \times 5$ mm^3 LSO:Ce cod. 0.4% Ca (Agile) and coupled to two single Hamamatsu S13360-3050-PE photo-detectors, have been connected to the two FEBs and acquired in coincidence, upon excitation with a ^{22}Na source. The FWHM of the resulting delay histogram has been evaluated in 125 ps. This value divided by $\sqrt{2}$ represents the contribution to CTR from one of the two scintillators. Then, the same procedure has been repeated after replacing one of these assembly crystal + photo-detector with the reference one. Subtracting of the previously evaluated contribution of one LSO:Ce cod. 0.4% Ca crystal from the width of the resulting histogram, the contribution to CTR of the reference detector has been evaluated in 88 ps FWHM.

Finally, it has to be remarked here that all the experimental setups described in this section are contained in a light tight box, where temperature is kept constant at 20 °C degrees by means of a dedicated cooling system.
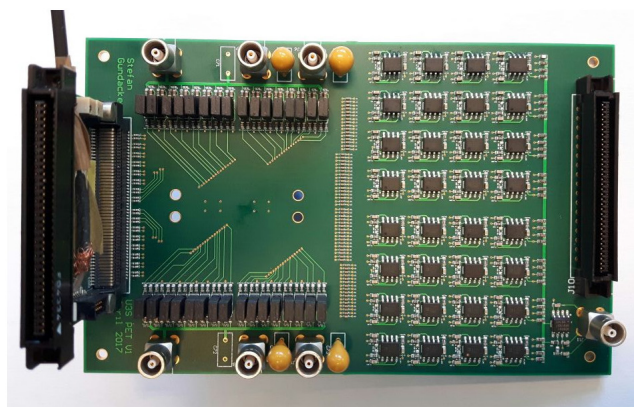
Figure 8. One of the two custom FEBs developed for this study. On the right, the array of 32 amplifiers, on the left, a NINO32 ASIC plugged into the board. The two Samtech connectors are placed on the rear side of the board (not visible in this picture).
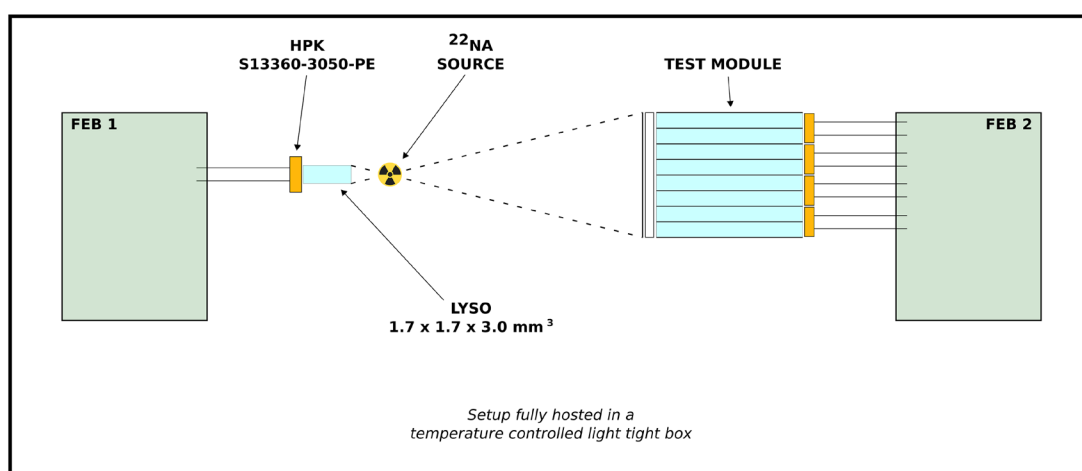

Figure 9. Schematic representation of the setup used to evaluate individual modules. A ^{22}Na source is placed between an external reference detector (left) and the module under study.

2.5. Module characterization procedure

The characterization of each module consists in a calibration run followed by an acquisition that evaluates the timing performance. Both measurements are performed exactly in the same conditions and with the same experimental apparatus, i.e. by means of an external reference crystal as described in section 2.4.

In the calibration run, first a simple charge spectrum of the reference crystal is built and the events outside of the 511 keV photopeak are discarded. Then for the remaining events the values of (u, v, w) coordinates calculated in the module are drawn in a 3D plot. Several accumulation volumes can be identified and separated (see figure 10) by means of a custom clustering algorithm (Stringhini *et al* 2016). The volumes obtained are used to identify the gamma rays interacting with individual crystals. Events whose (u, v, w) coordinates fall outside of these regions can be interpreted as inter-crystal scatters, i.e. events where a single gamma ray is depositing its energy in more than one crystal. For the purpose of this study, these events are discarded.

When histograms of the total amount of light collected by the photo-detectors, P, are plotted for events confined in each volume, the charge spectrum of each crystal in the module can be reconstructed, as shown for example in figure 11, allowing to determine the ranges of photopeak selection, and at the same time to evaluate the energy resolutions. Once the events in the photopeak of individual crystals are sorted, an accurate calibration curve that allows to reconstruct the physical coordinate of the DOI position from the value of w can be obtained for each scintillator, as it was demonstrated in a previous work (Stringhini *et al* 2016). At the same time, also the DOI resolution can be evaluated. Subsequently, a 2D histogram of $(t_1 - t_i)$ versus w is built for each $D_{i \neq 1}$, like the one shown in figure 2, and the experimental relations $g_i(w)$ are obtained. Finally, a 2D scatter plot of $t_1 - t_{ref}$ versus w is produced, to derive $d(w)$.

Once the calibration data is available, an acquisition to evaluate CTR is performed. Each event is processed and assigned to a particular crystal in the module, then only the ones simultaneously in the photopeak of both this crystal and the reference one are taken into account. Subsequently, two delay histograms are built. The first,
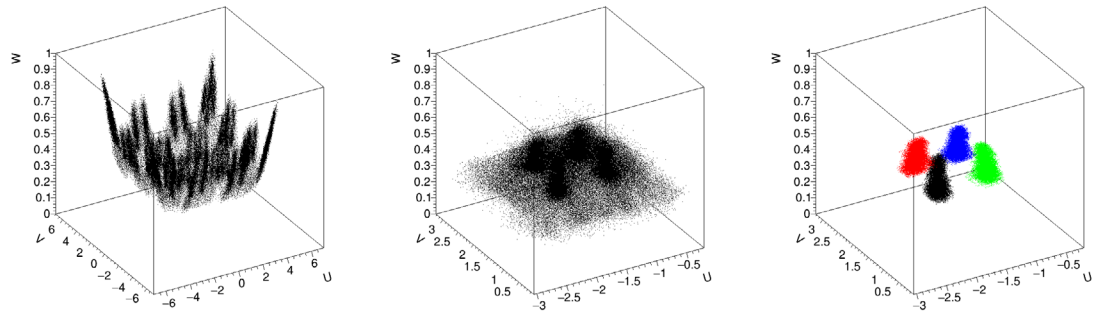
Figure 10. Example illustrating the procedure of crystal separation. First, a 3D histogram of all the events of a calibration run is plotted for a particular module (left). 64 accumulation volumes can be distinguished. To help visualization, here the histogram has been zoomed to a (u, v) area corresponding to the crystals coupled to a single individual MPPC, in this case C2 defined in figure 6 (center). The clustering then performs the separation by starting from a seed defined as the voxel with the highest number of counts C_0. It then analyses all the nearby voxels, discarding the ones with a number of counts lower then a threshold defined as a fraction of C_0, and adding the others to the list of seeds. The procedure is then repeated recursively for all the seeds, paying attention to avoid running more then once on the same seed. When no more new seeds are found, the volume represented by the collection of all seeds defines a cluster. These voxels are then removed from the 3D histogram, and the procedure starts again, until 64 clusters are found. The effect of this algorithm on the central plot is shown in the plot on the right, where four regions are clearly separated.
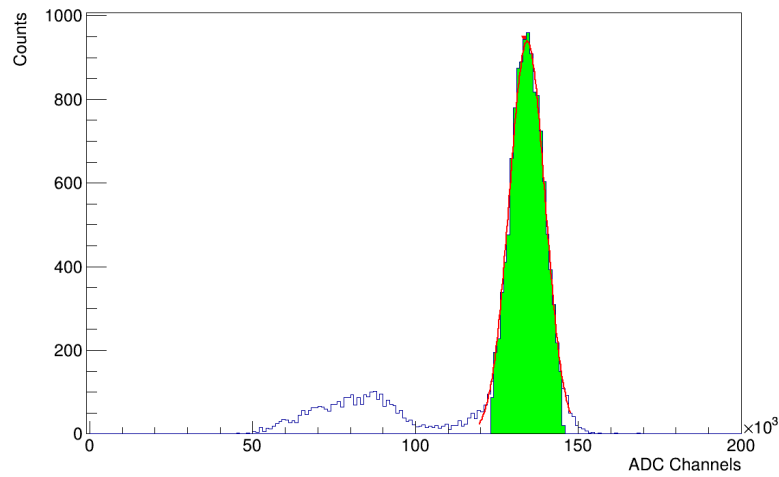

Figure 11. Example of the charge spectrum obtained for one crystal in a test module. In this particular case, the crystal belongs to a 8×8 crystal matrix coupled with a 4×4 photo-detector array. The area highlighted in green corresponds to a typical cut for the photopeak range of $\pm 2\sigma$.

H_{std} is constructed without taking advantage of the DOI correction, i.e. it is filled with the difference between the timestamp t_1 of the photo-detector coupled to the crystal of interaction, and t_{ref}, the timestamp of the reference crystal
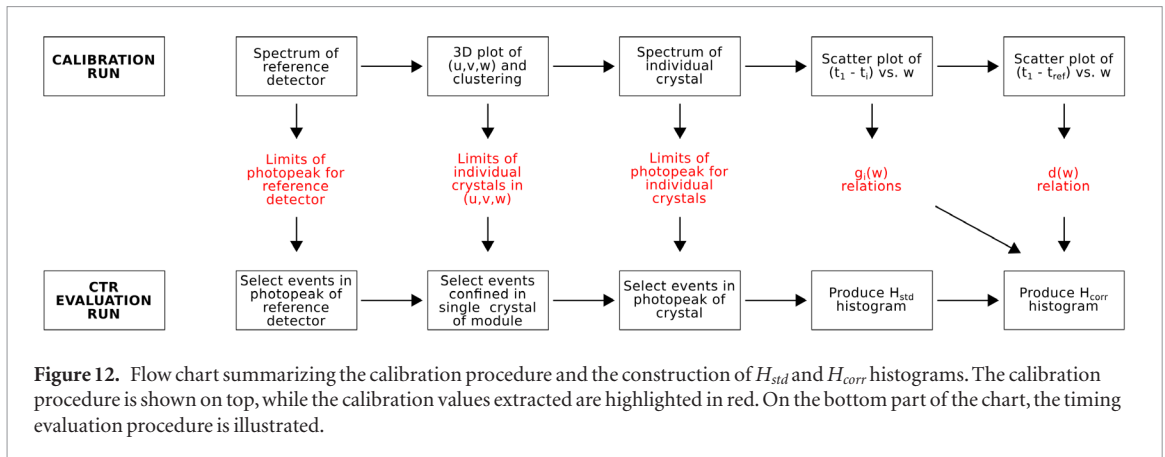
$$\Delta t_{std} = t_1 - t_{ref}. \tag{7}$$

The second one, H_{corr}, exploits the DOI correction method proposed in section 2.2, by using

$$\Delta t_{corr} = \hat{\theta}_{in} - t_{ref}, \tag{8}$$

where $\hat{\theta}_{in}$ is defined in equation (6). A flow chart to summarize the calibration procedure and the construction of H_{std} and H_{corr} is shown in figure 12. The H_{std} and H_{corr} distributions are fitted with an exponentially modified Gaussian distribution

$$G_e(t; \mu, \sigma, \lambda) = \frac{\lambda}{2} \cdot \exp \frac{\lambda}{2}(2\mu + \lambda\sigma^2 - 2t) \cdot E\left(\frac{\mu + \lambda\sigma^2 - t}{\sqrt{2}\sigma}\right), \tag{9}$$

where μ is the mean value and σ the standard deviation of the Gaussian component, λ is the rate of the exponential part and E is the complementary error function. The function $G_e(t; \mu, \sigma, \lambda)$ does not have any physical meaning and it has been used only to decouple from statistical fluctuations while taking into account possible asymmetries in the histograms. The FWHM is measured directly on the fitted functions, the contribution to CTR of the reference crystal is subtracted and the result multiplied by $\sqrt{2}$, to obtain the timing resolutions without DOI correction, CTR_{std}, and with DOI correction, CTR_{corr}, of a system made by

Figure 12. Flow chart summarizing the calibration procedure and the construction of H_{std} and H_{corr} histograms. The calibration procedure is shown on top, while the calibration values extracted are highlighted in red. On the bottom part of the chart, the timing evaluation procedure is illustrated.

two modules identical to the one under study. Two examples of the delay histograms recorded for one crystal in a 4×4 and one in a 8×8 DOI module are shown in figure 13, before and after correction, to give a visual representation of the improvement in CTR.

3. Results

For each individual scintillator of every DOI module in table 1, a charge spectrum has been constructed from the values of total light collected, as defined in equation (1). The position of 511 keV photopeak provides an evaluation of the total light collection for the crystal, in units of ADC channels. The energy resolution is evaluated from the FWHM of the photopeak itself. Finally, the timing resolutions, CTR_{std} and CTR_{corr}, have been calculated with the procedure described in section 2.5. The same strategy has been applied to reference modules, with the notable difference that, since no DOI information is available, only CTR_{std} can be calculated. Since the two types of array under study, with 8×8 and 4×4 scintillators, are interesting for different applications, the results of their characterization are presented in more details in separate sections.

3.1. 8×8 modules

The average light collection and energy resolution measured for all the crystals in the two 8×8 DOI modules (D.64.1 and D.64.2) have been evaluated in $(115 \pm 3) \times 10^3$ ADC channels, and $9.9\% \pm 0.2\%$ FWHM. If only the 16 scintillators coupled to the four central MPPCs (i.e. to B2, C2, B3, and C3 in figure 6) are considered, this averages become $(127 \pm 3) \times 10^3$ ADC channels, and $8.9\% \pm 0.2\%$ FWHM. This is expected, since the total amount of light collected by the MPPC array depends on the position of the crystal of interaction with respect to the MPPC array itself, with better light collection the closer the crystal is to the center. Total light collection and energy resolution are clearly anti-correlated, as shown for example in figure 14, for one 8×8 DOI module. Overall, both light collection and energy resolution values obtained for the DOI modules are very similar to the ones measured for the corresponding reference modules (R.64.1 and R.64.2). In particular, averages of $(118 \pm 3) \times 10^3$ ADC channels and $9.9\% \pm 0.2\%$ FWHM were found for all the 64 scintillators, while $(132 \pm 3) \times 10^3$ ADC channels and $9.0\% \pm 0.2\%$ FWHM for central ones.

The average standard CTR_{std}, before applying the timing correction method, measured on the two arrays was 307 ± 3 ps FWHM for all the scintillators, and 308 ± 3 ps FWHM on central scintillators, and it improved to 166 ± 2 ps FWHM, and 157 ± 2 ps FWHM, respectively, after timing correction (see figure 15). The improvement is therefore in the order of 140 ps, and a slight dependence on the position of the crystal with respect to the MPPC array is observed, similarly to what has been found for energy resolution (see figure 16). The correction method relies on the measurement of the $g_i(w)$ relations defined in equation (3). For the four central MPPCs, eight such relations can be obtained, while only three for the MPPCs in the corners of the array, and five for all the others. As a consequence, the performance of the correction is expected to be better for the crystals coupled to the central MPPCs, as it is experimentally verified. The magnitude of this performance degradation on the borders of the modules is anyway just in the order of a few picoseconds. As a comparison, in reference modules, the average CTR_{std} was evaluated in 158 ± 2 ps and 154 ± 2 ps for all and central scintillators, respectively. A summary of the performance of 8×8 DOI and reference modules can be found in table 2.

3.2. 4×4 modules

The spatial distribution of light collection and energy resolution measured for one of the two 4×4 DOI modules (D.16.1 and D.16.2) is shown in figure 17. The distributions of measured timing resolutions before and after timing correction are shown in figure 18, while their spatial distribution can be seen in figure 19. Similarly to
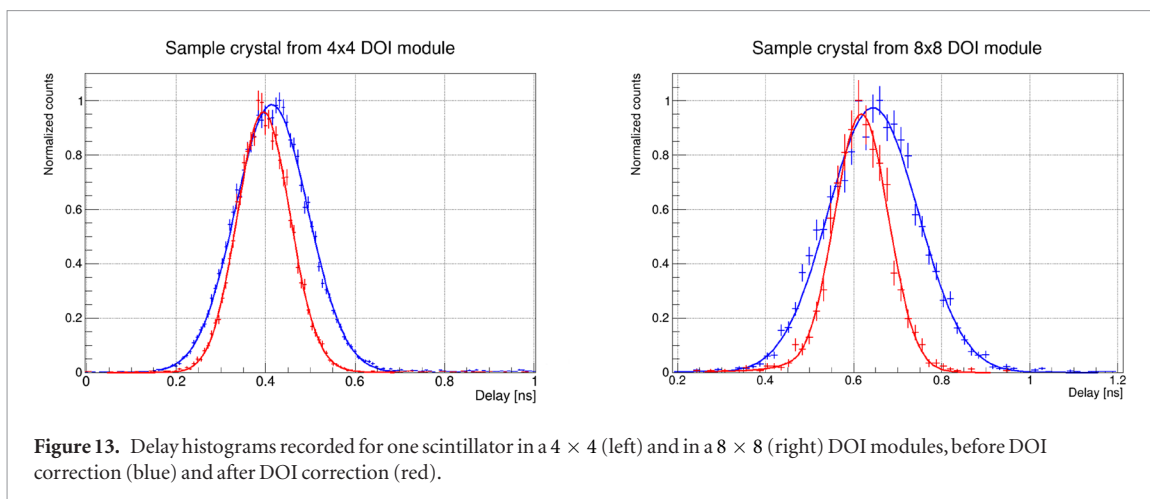
Figure 13. Delay histograms recorded for one scintillator in a 4×4 (left) and in a 8×8 (right) DOI modules, before DOI correction (blue) and after DOI correction (red).
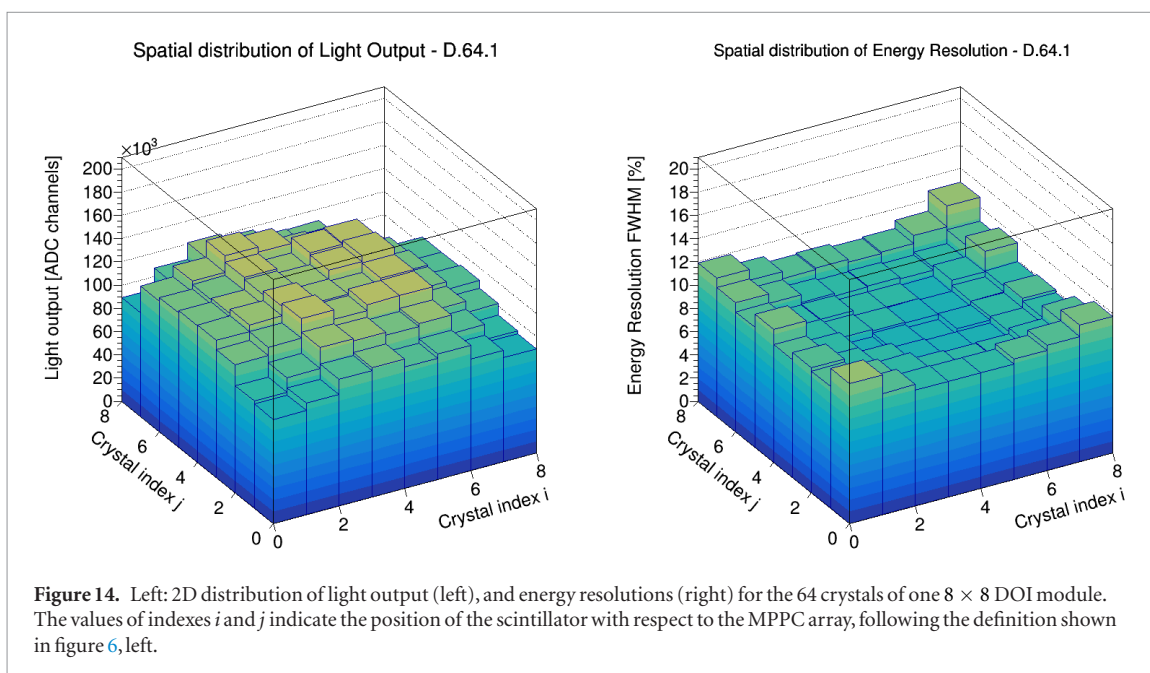

Figure 14. Left: 2D distribution of light output (left), and energy resolutions (right) for the 64 crystals of one 8×8 DOI module. The values of indexes i and j indicate the position of the scintillator with respect to the MPPC array, following the definition shown in figure 6, left.
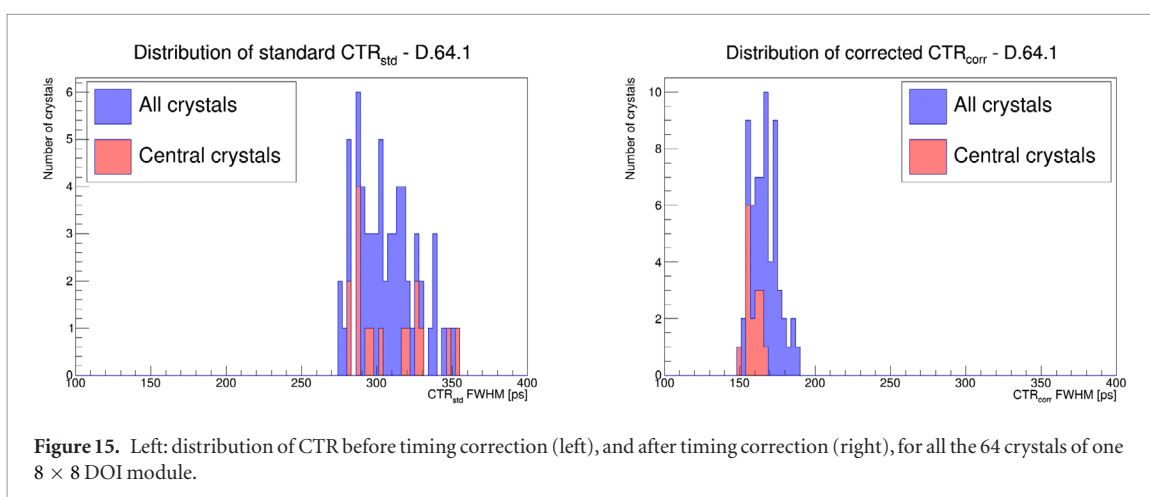
Figure 15. Left: distribution of CTR before timing correction (left), and after timing correction (right), for all the 64 crystals of one 8×8 DOI module.

what has been found for 8×8 modules, light collection, energy resolution and CTR_{corr} are better for crystals coupled to the four central MPPCs.

Average light collection and energy resolution were estimated in $(134 \pm 3) \times 10^3$ ADC channels and $9.5\% \pm 0.2\%$ FWHM, when averaging on all the scintillators of both 4×4 DOI modules, and $(154 \pm 3) \times 10^3$ ADC channels and $8.8\% \pm 0.2\%$ FWHM when considering only the central channels. In the two 4×4 reference

Figure 16. Left: 2D distribution of of CTR before timing correction (left), and after timing correction (right), for all the 64 crystals of one 8×8 DOI module. The values of indexes i and j indicate the position of the scintillator with respect to the MPPC array, following the definition shown in figure 6, left.
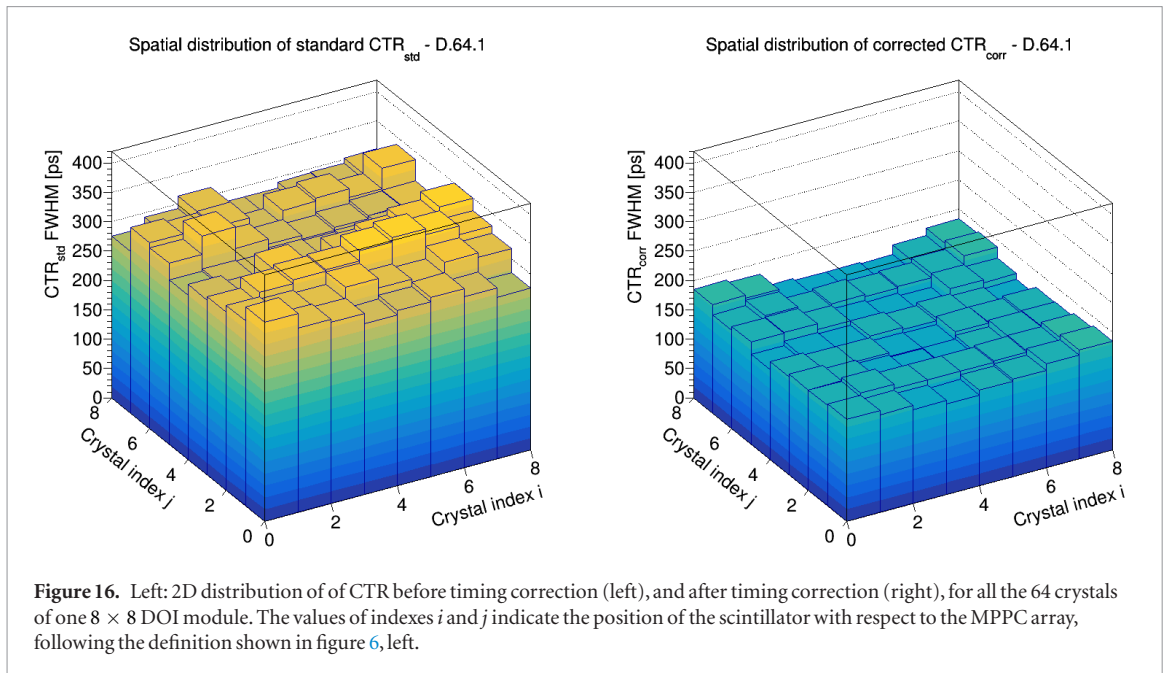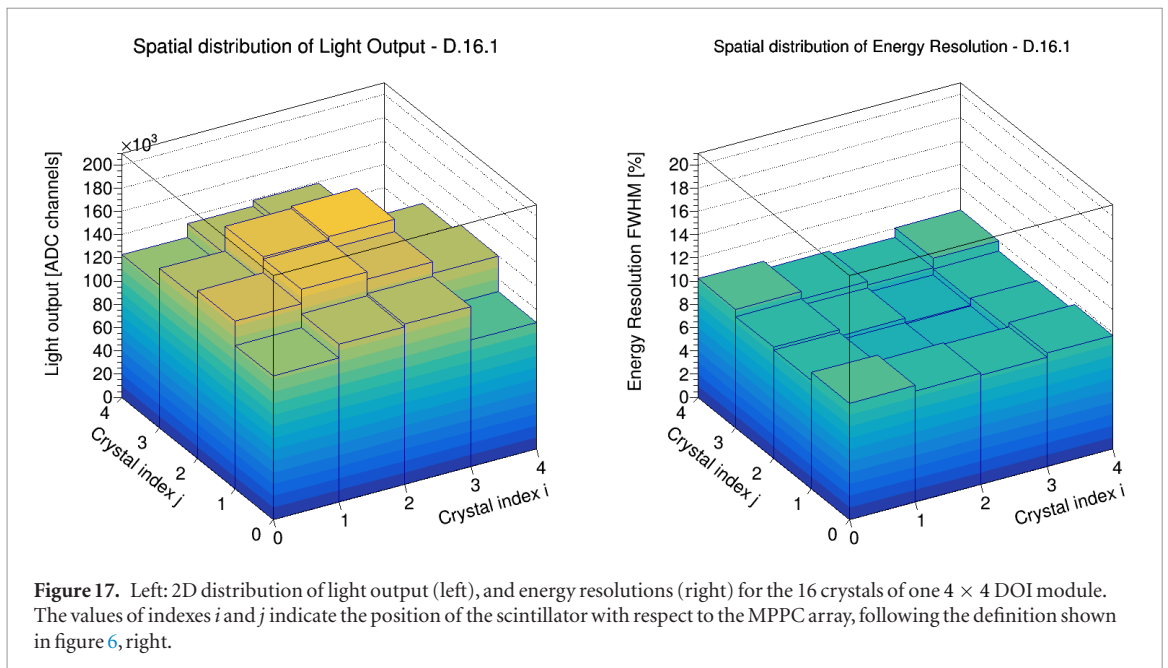
Table 2. Average values of light output, energy resolution and CTR (standard and corrected) measured for the two types of DOI and reference modules. Central crystals are defined as the scintillators coupled to MPPCs B2, C2, B3, and C3 in figure 6. Light output is reported in thousands of ADC channels (kCh). All values of energy and timing resolution are given in FWHM.

| Array type | Crystals | DOI modules | | | | Reference modules | | |
		L. O. (kCh)	En. res. (%)	CTR_{std} (ps)	CTR_{corr} (ps)	L. O. (kCh)	En. res. (%)	CTR_{std} (ps)
8×8	All	115 ± 3	9.9 ± 0.2	307 ± 3	166 ± 2	118 ± 3	9.9 ± 0.2	158 ± 2
	Central	127 ± 3	8.9 ± 0.2	308 ± 3	157 ± 2	132 ± 3	9.0 ± 0.2	154 ± 2
4×4	All	134 ± 3	9.5 ± 0.2	233 ± 2	165 ± 2	139 ± 3	9.5 ± 0.2	162 ± 2
	Central	154 ± 3	8.8 ± 0.2	234 ± 2	159 ± 2	155 ± 3	9.0 ± 0.2	158 ± 2

Figure 17. Left: 2D distribution of light output (left), and energy resolutions (right) for the 16 crystals of one 4×4 DOI module. The values of indexes i and j indicate the position of the scintillator with respect to the MPPC array, following the definition shown in figure 6, right.

modules (R.16.1 and R.16.2), the values of $(139 \pm 3) \times 10^3$ ADC channels and $9.5\% \pm 0.2\%$ FWHM were found for all crystals, while (155 ± 3) and $9.0\% \pm 0.2\%$ FWHM for central crystals.

The average value of CTRs among all the crystals of the two 4×4 DOI modules was measured in 233 ± 2 ps FWHM before timing correction, and 165 ± 2 ps FWHM after timing correction. For crystals coupled to central MPPCs, the values were 234 ± 2 ps FWHM and 159 ± 2. For comparison, the average CTR_{std} measured in the two reference modules was 162 ± 2 ps FWHM for all crystals, and 158 ± 2 for the four central ones. A summary of
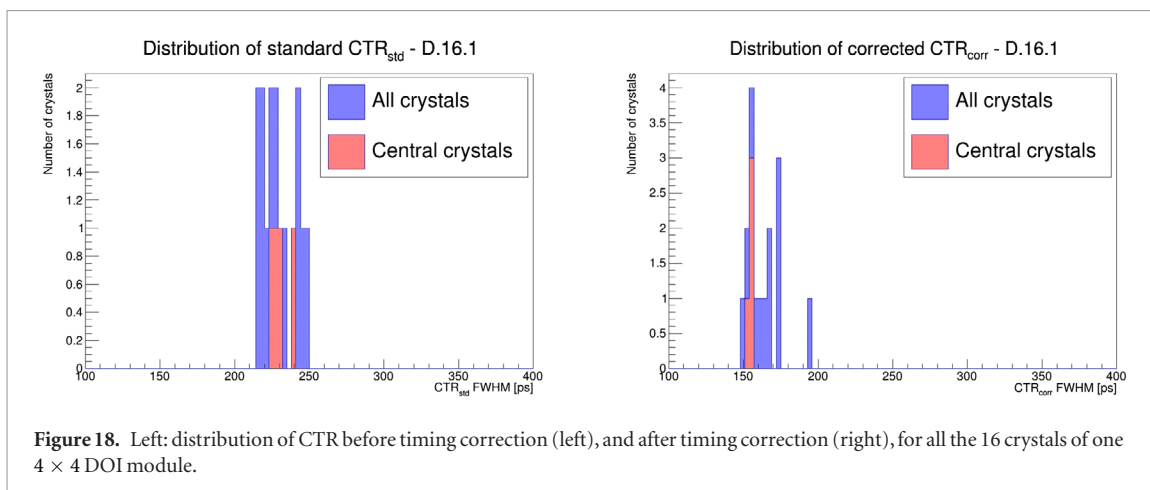
Figure 18. Left: distribution of CTR before timing correction (left), and after timing correction (right), for all the 16 crystals of one 4 × 4 DOI module.
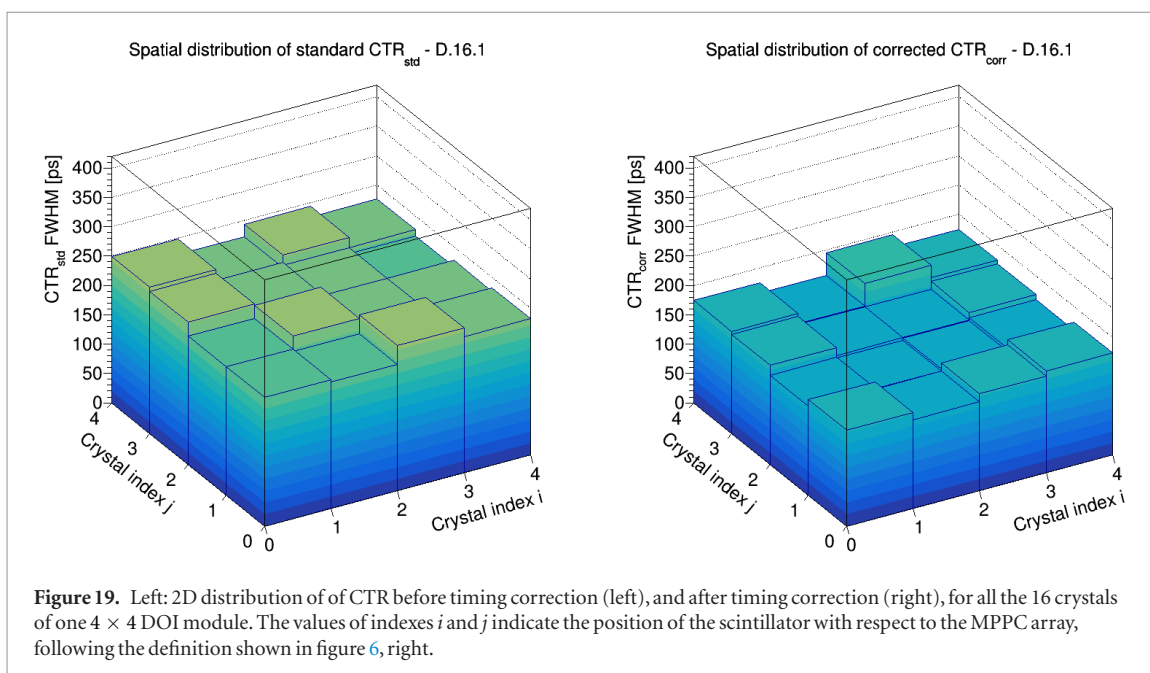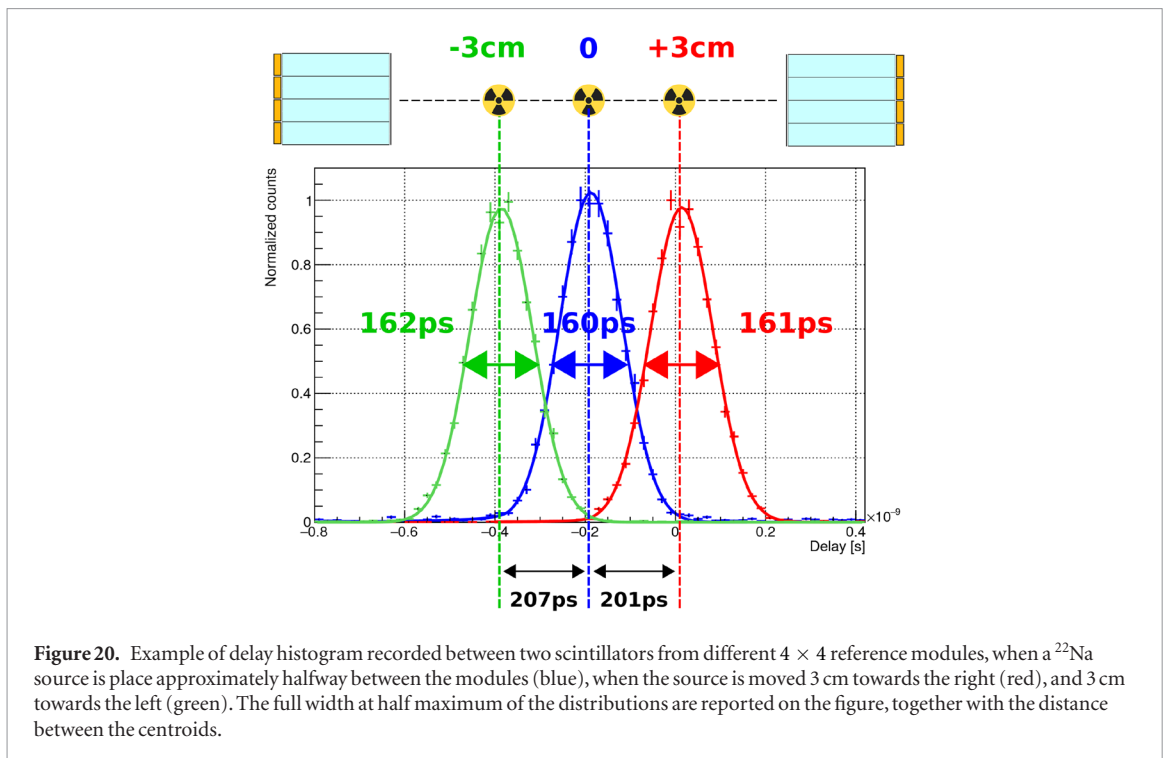

Figure 19. Left: 2D distribution of of CTR before timing correction (left), and after timing correction (right), for all the 16 crystals of one 4 × 4 DOI module. The values of indexes *i* and *j* indicate the position of the scintillator with respect to the MPPC array, following the definition shown in figure 6, right.

the performance of 4 × 4 DOI and reference modules can be found in table 2, together with the results of 8 × 8 modules.

4. Discussion

The results shown in the previous sections are summarized in table 2. The performance of 8 × 8 DOI modules is particularly interesting in view of the possible development of a high resolution PET scanner targeted for small animals, or specific organs in human body, where high levels of spatial resolutions are required. The combination of the small cross-section of scintillators (individual area of $1.53 \times 1.53 \text{ mm}^2$) to the already demonstrated DOI resolution of 3 mm FWHM (Stringhini *et al* 2016), in fact, is considered sufficient to provide an homogeneous spatial resolution at the level of the physical limits imposed by positron range (i.e. in the order of 1.5 mm FWHM for positrons emitted by ^{18}F-based radio-tracers). The 4 × 4 DOI configuration, instead, is more suited for comparison to the case of whole-body PET scanners, where high granularity is not required.

In general, slightly better performances have been found for the crystals coupled to the central MPPCs of the photo-detector array (i.e. B2, B3, C2 and C3 in figure 6), in terms of total light collection, energy resolution, and timing resolution. This difference can be explained, as already mentioned, with the non homogeneous light collection due to the finite dimensions of the 4 × 4 MPPC arrays. Anyway, this performance degradation remains very small, even for the crystals in the corners of the modules. Nevertheless, in discussing the results we will focus on the measurements obtained on scintillators coupled to the central MPPCs. The ultimate goal of this research, in fact, is to develop a module structure that can be instrumental to the development of a full PET detector. In such a scanner, several modules would have to be used, to cover a reasonable portion of the solid angle around the region of interest, and reach acceptable levels of sensitivity. The light sharing mechanism at the basis of this work

Figure 20. Example of delay histogram recorded between two scintillators from different 4 × 4 reference modules, when a ^{22}Na source is place approximately halfway between the modules (blue), when the source is moved 3 cm towards the right (red), and 3 cm towards the left (green). The full width at half maximum of the distributions are reported on the figure, together with the distance between the centroids.

can easily be allowed between different modules, for example adopting a common light guide, and common optical coupling materials. This would be especially feasible in a flat scanner configuration, where two parallel plates are adopted, like for example in the ClearPEM breast scanner (Bugalho *et al* 2009), but also in cylindrical PET systems built by repetition of flat sections. As a result, only a few channels on the border of the detector would found themselves in the conditions experienced by the 12 border MPPCs of an Hamamatsu S13361-3050-AE-04 array. In a single module, central MPPCs represents only the 25% of all the channels. Even in a rather small plate, made for example of 100 DOI modules arranged in a 10 × 10 matrix (for a total section of section of about 13 × 13 cm^2, considering some margin), 90% of the MPPCs would be in the same conditions of the central channels of an individual module. The performance degradation due to border channels, already small in test modules, would be therefore negligible.

The light output has been found to be very similar between DOI and reference modules, both in 4 × 4 and 8 × 8 arrays. The main factors limiting light extraction are different between the two module structures. In particular, in DOI modules the presence of a light guide is expected to cause some amount of light loss, and at the same time optical photons are more likely to be absorbed by surface imperfections due to depolishing. In reference modules, instead, part of the light emitted upon scintillation is inevitably trapped inside the crystal, as a result of the combination of specular reflection (due to the polished surfaces) and the rectangular parallelepipedous shape of the scintillator. This limitation is not present in DOI modules, where the reflection of optical photons on lateral surfaces is in general not specular, due to the depolished finishing. The results in table 2 demonstrate that these factors on average are balancing out, and in both the 8 × 8 and the 4 × 4 modules no significant difference has been measured between the light output of DOI and reference configurations. The light output of 8 × 8 modules, instead, is in general lower (about 15%) with respect to 4 × 4 modules. This is a known consequence of the higher aspect ratio of small cross-section scintillators, that makes light extraction less efficient, as already reported in literature in the past (Auffray *et al* 2013). As expected, energy resolution does not degrade between reference and DOI modules, as an effect of the similar light collection. The lower light output of 8 × 8 modules does not reflect in a degraded energy resolution, and on average resolutions around 9% FWHM at 511 keV photopeak have been found in all the configurations tested.

Excellent levels of performance have been measured in term of timing resolution in both reference and DOI modules, and a consistent improvement in CTR, similar to the one shown in figure 13, has been found for all the scintillators in each DOI module upon application of the timing correction method described in section 2.2. In order to ensure the correctness of the procedure adopted to estimate the timing resolution, and especially to validate the absolute values of CTR ∼160 ps FWHM presented in table 2, a coincidence acquisition was performed between the two reference modules R.16.1 and R.16.2. The purpose is to measure directly the width of delay histograms acquired in coincidence between arrays, without the need to estimate it after the subtraction of the contribution of the external reference detector. The experimental setup is the same described in figure 9, but with one reference module plugged into each FEB, while the ^{22}Na source is placed approximately halfway

between them. For each pair of crystals, one for each module, events with simultaneous 511 keV depositions are selected and a delay histogram is built. An example is represented by the blue histogram in figure 20. The average CTR measured on such histograms, for all the possible pairs of scintillators among the four central ones of both the modules, was evaluated in 160 ± 2 ps FWHM. This value is compatible with the ones reported in table 2, and demonstrate the quantitative correctness of the procedure to estimate the timing resolution of the modules. Furthermore, we repeated the same measurement displacing the ^{22}Na source by 3 cm along the line connecting the two modules, first in one direction, then in the opposite one. The centroid of the delay histograms moved accordingly by $\sim$200 ps, as expected (green and red histograms in figure 20). The peaks can be clearly separated, giving a visual confirmation of the resolving power achieved with the setup.

A general degradation of CTR when passing from reference to DOI modules has been found, if the non-corrected, standard CTR_{std} is considered, i.e. when the resolution is calculated only on the basis of the signal of the photo-detector D_1 coupled to the crystal of interaction. This is expected, since while almost all the light reaches this photo-detector in the case of reference modules, a consistent portion (in general between 40% and 60%) is shared to the neighboring channels in DOI modules. The degradation of CTR_{std} is more consistent in the case of 8×8 modules, where the higher aspect ratio results in a larger mean number of interactions for the optical photons with the lateral surfaces of the scintillators, before having a chance to be extracted. This, combined with the modification to the directions of photons introduced by the depolishing, increases the spread in the travel path of the photons, deteriorating the timing performance. When the entire information carried by the optical photons is taken into account, however, by means of the proposed timing correction method, the CTR is recovered, and an average CTR_{corr} of 159 ± 2 ps FWHM and 157 ± 2 ps FWHM is reached with 4×4 and 8×8 DOI modules, respectively. Both values are compatible with the ones obtained with reference modules.

5. Conclusions

We developed a 64-channels readout setup with excellent timing resolution, to test the performance of a DOI extraction method, previously proposed by our group, based on light sharing. At the same time, we proposed and tested a method to improve the CTR in this configuration, by combining the timestamps extracted by the individual detector channels with the use of the DOI information. The results obtained demonstrate that it is possible to achieve a timing resolution below 160 ps FWHM in a structure based on 15 mm long LYSO:Ce scintillators, while simultaneously providing a spatial resolution of 1.5 mm FWHM, a DOI resolution of 3 mm FWHM, and an energy resolution of 9% FWHM, as already demonstrated in previous works. These levels of performance, coupled to the inherent simplicity of the module structure, and the relatively low production costs due to the single side readout, make this method particularly attractive for the development of a high resolution PET scanner. Furthermore, the values of CTR obtained after timing correction on all tested samples, demonstrate that this configuration allows to extract DOI information without intrinsically degrading the timing performance, with respect to a standard module of the same crystal dimensions but without DOI capability. The light sharing scheme presented in section 2.1, combined with the method described in section 2.2, could represents therefore a viable solution to overcome the physical limitations of CTR due to the mismatch of speed between gamma rays and optical photons in dense scintillators.

Acknowledgments

ORCID iDs

S Gundacker ⬥ https://orcid.org/0000-0003-2087-3266

References

Anghinolfi F, Jarron P, Martemyanov A N, Usenko E, Wenninger H, Williams M C S and Zichichi A 2004 NINO: an ultra-fast and low-power front-end amplifier/discriminator ASIC designed for the multigap resistive plate chamber *Nucl. Instrum. Meth.* A **533** 183–7

Auffray E *et al* 2013 A comprehensive & systematic study of coincidence time resolution and light yield using scintillators of different size and wrapping *IEEE Trans. Nucl. Sci.* **60** 3163–71

Berg E, Roncali E, Kapusta M, Du J and Cherry S R 2016 A combined time-of-flight and depth-of-interaction detector for total-body positron emission tomography *Med. Phys.* **43** 939–50

Bläckberg L, Moebius M, El Fakhri G, Mazur E and Sabet H 2018 Light spread manipulation in scintillators using laser induced optical barriers *IEEE Trans. Nucl. Sci.* **65** 2208–15

Borghi G *et al* 2016 TOF-PET imaging with sub-3 mm resolution and 215 ps coincidence resolving time using digital SIPM based monolithic scintillator detectors in a 70 cm diameter tomographic setup *J. Nucl. Med.* **57** 104

Bugalho R *et al* 2009 Experimental characterization of the clear-PEM scanner spectrometric performance *J. Instrum.* **4** P10011

Conti M 2011 Focus on time-of-flight PET: the benefits of improved time resolution *Eur. J. Nucl. Med. Mol. Imaging* **38** 1147–57

Defrise M, Rezaei A and Nuyts J 2012 Time-of-flight pet data determine the attenuation sinogram up to a constant *Phys. Med. Biol.* **57** 885

Del Guerra A, Belcari N and Bisogni M 2016 Positron emission tomography: its 65 years *La Rivista Del Nuovo Cimento* **39** 155–223

Gundacker S, Acerbi F, Auffray E, Ferri A, Gola A, Nemallapudi M, Paternoster G, Piemonte C and Lecoq P 2016 State of the art timing in TOF-PET detectors with LuAG, GAGG and L(Y)SO scintillators of various sizes coupled to FBK-SiPMS *J. Instrum.* **11** P08008

Gundacker S, Knapitsch A, Auffray E, Jarron P, Meyer T and Lecoq P 2014 Time resolution deterioration with increasing crystal length in a TOF-PET system *Nucl. Instrum. Methods Phys. Res.* A **737** 92–100

Ito M, Lee J S, Kwon S I, Lee G S, Hong B, Lee K S, Sim K S, Lee S J, Rhee J T and Hong S J 2010 A four-layer DOI detector with a relative offset for use in an animal PET system *IEEE Trans. Nucl. Sci.* **57** 976–81

Ito M, Lee M S and Lee J S 2013 Continuous depth-of-interaction measurement in a single-layer pixelated crystal array using a single-ended readout *Phys. Med. Biol.* **58** 1269

Karp J S and Daube-Witherspoon M E 1987 Depth-of-interaction determination in NaI(Tl) and BGO scintillation crystals using a temperature gradient *Nucl. Instrum. Methods Phys. Res.* A **260** 509–17

Kolb A, Parl C, Mantlik F, Liu C C, Lorenz E, Renker D and Pichler B J 2014 Development of a novel depth of interaction PET detector using highly multiplexed G-APD cross-strip encoding *Med. Phys.* **41** 081916

Kwon S I, Ferri A, Gola A, Berg E, Piemonte C, Cherry S R and Roncali E 2016 Reaching 200 ps timing resolution in a time-of-flight and depth-of-interaction positron emission tomography detector using phosphor-coated crystals and high-density silicon photomultipliers *J. Med. Imaging* **3** 043501

Lecoq P 2017 Pushing the limits in time-of-flight PET imaging *IEEE Trans. Rad. Plasma Med. Sci.* **1** 473–85

Levin C 2002 Design of a high-resolution and high-sensitivity scintillation crystal array for PET with nearly complete light collection *IEEE Trans. Nucl. Sci.* **49** 2236–43

Liu H, Omura T, Watanabe M and Yamashita T 2001 Development of a depth of interaction detector for x-rays *Nucl. Instrum. Methods Phys. Res.* A **459** 182–90

Marcinkowski R, Mollet P, Holen R V and Vandenberghe S 2016 Sub-millimetre DOI detector based on monolithic LYSO and digital SIPM for a dedicated small-animal PET system *Phys. Med. Biol.* **61** 2196

Miller M, Zhang J, Binzel K, Griesmer J, Laurence T, Narayanan M, Natarajamani D, Wang S and Knopp M 2015 Characterization of the Vereos digital photon counting PET system *J. Nucl. Med.* **56** 434

Miyaoka R S, Lewellen T K, Yu H and McDaniel D L 1998 Design of a depth of interaction (DOI) PET detector module *IEEE Trans. Nucl. Sci.* **45** 1069–73

Moses W W and Derenzo S E 1999 Prospects for time-of-flight PET using LSO scintillator *IEEE Trans. Nucl. Sci.* **46** 474–8

Otte A N, Barral J, Dolgoshein B, Hose J, Klemin S, Lorenz E, Mirzoyan R, Popova E and Teshima M 2005 A test of silicon photomultipliers as readout for PET *Nucl. Instrum. Methods Phys. Res.* A **545** 705–15

Pizzichemi M, Stringhini G, Niknejad T, Liu Z, Lecoq P, Tavernier S, Varela J, Paganoni M and Auffray E 2016 A new method for depth of interaction determination in PET detectors *Phys. Med. Biol.* **61** 4679

Seifert S and Schaart D R 2015 Improving the time resolution of TOF-PET detectors by double-sided readout *IEEE Trans. Nucl. Sci.* **62** 3–11

Shibuya K, Nishikido F, Tsuda T, Kobayashi T, Lam C, Yamaya T, Yoshida E, Inadama N and Murayama H 2008 Timing resolution improvement using DOI information in a four-layer scintillation detector for TOF-PET *Nucl. Instrum. Methods Phys. Res.* A **593** 572–7

Shimazoe K, Choghadi A, Takahashi H and Watanabe K 2016 Single side readout depth of interaction method with wavelength discrimination *IEEE Trans. Nucl. Sci.* **63** 679–84

Stringhini G, Pizzichemi M, Ghezzi A, Stojkovic A, Paganoni M and Auffray E 2016 Development and evaluation of a practical method to measure the depth of interaction function for a single side readout PET detector *J. Instrum.* **11** P11014

Toussaint M, Loignon-Houle F, Dussault J and Lecomte R 2019 Analytical model of DOI-induced time bias in ultra-fast scintillation detectors for TOF-PET *Phys. Med. Biol.* **64** 065009

Trummer J, Auffray E and Lecoq P 2009 Depth of interaction resolution of LuAP and {LYSO} crystals *Nucl. Instrum. Methods Phys. Res.* A **599** 264–9

Uchida H, Sakai T, Yamauchi H, Hakamata K, Shimizu K and Yamashita T 2016 A novel single-ended readout depth-of-interaction PET detector fabricated using sub-surface laser engraving *Phys. Med. Biol.* **61** 6635

van Sluis J J, de Jong J, Schaar J, Noordzij W, van Snick P, Dierckx R, Borra R, Willemsen A and Boellaard R 2019 Performance characteristics of the digital biograph vision PET/CT system *J. Nucl. Med.* preprint (https://doi.org/10.2967/jnumed.118.215418)

Vilardi I *et al* 2006 Optimization of the effective light attenuation length of YAP:Ce and LYSO:Ce crystals for a novel geometrical PET concept *Nucl. Instrum. Methods Phys. Res.* A **564** 506–14

Vinke R, Olcott P D, Cates J W and Levin C S 2014 The lower timing resolution bound for scintillators with non-negligible optical photon transport time in time-of-flight PET *Phys. Med. Biol.* **59** 6215

Wiener R, Surti S and Karp J 2013 DOI determination by rise time discrimination in single-ended readout for TOF PET imaging *IEEE Trans. Nucl. Sci.* **60** 1478–86

Yang Y, Wu Y and Cherry S R 2009 Investigation of depth of interaction encoding for a pixelated LSO array with a single multi-channel PMT *IEEE Trans. Nucl. Sci.* **56** 2594–9

Ziemons K *et al* 2005 The clearpet project: development of a 2nd generation high-performance small animal PET scanner *Nucl. Instrum. Methods Phys. Res.* A **537** 307–11